Parametric Enhancement of Radiation from Electrically Small Antennas

Ahmed Mekawy, Huanan Li, Younes Radi, and Andrea Alù

Phys. Rev. Applied **15**, 054063 — Published 27 May 2021

DOI: 10.1103/PhysRevApplied.15.054063

Parametric enhancement of radiation from electrically small antennas

Ahmed Mekawy[1,2], Huanan Li[1], Younes Radi[1], Andrea Alù[1,2,3,*]

[1]*Photonics Initiative, Advanced Science Research Center, City University of New York, New York, NY 10031, USA*

[2]*Department of Electrical Engineering, City College of The City University of New York, New York, NY 10031, USA*

[3]*Physics Program, Graduate Center, City University of New York, New York, NY 10016, USA*

[*]*aalu@gc.cuny.edu*

Electrically small antennas are characterized by large quality factors, which yield limited gain-bandwidth products as a result of the Bode-Fano limit. This bound implies a trade-off between antenna footprint and radiation features, hindering wireless applications that require compact, broadband and efficient antennas. Here, building on a previous theoretical analysis of parametric matching networks [Phys. Rev. Lett. 123, 164102 (2019)], we demonstrate how parametric phenomena can overcome this trade-off, offering a pathway to realize stable non-Foster wideband antennas that go beyond the restrictions of passive systems. We demonstrate our approach in a planar small loop antenna loaded by a time-varying capacitor that oscillates around twice the radiation frequency, showing that it can result in wideband radiation enhancement exceeding the limitations of passive scenarios.

Introduction—Electrically small antennas (ESAs) satisfy the relation $ka<\pi/2$, where k and a are respectively the free-space wavenumber and the radius of the smallest surrounding sphere [1],[2]. Although ESAs are critical components for compact wireless systems [3]-[7], they suffer a general trade-off between size and bandwidth. ESAs are characterized by a large ratio of the stored to radiated energy defining their quality factor Q: the smaller the antenna size, the higher its quality factor and the narrower its fractional bandwidth. For passive, linear, time-invariant ESAs, the Chu limit, Q_{Chu} defines the minimum attainable Q [8], and it scales with the antenna volume as $Q_{Chu}\approx 1/(ka)^3$ [9]. Consequently, while all other elements of modern electronics have been scaling to smaller dimensions, the footprint of today's wireless technology is dominated by the antenna size, which cannot be squeezed too much, given the ever-growing requirements on bandwidth.

This trade-off can be explained by examining the response of ESAs upon excitation at its input port. Due to the large mismatch between the source and ESA impedance (characterized by a large imaginary part corresponding to the large Q), most of the input power is generally reflected without the presence of a proper matching network. The gain-bandwidth product (G-BW) is defined as the spectral ratio of the radiated power $P_{rad}(\omega)$ normalized to the maximum input power $P_{in,max}(\omega)$, $|T| = P_{rad}(\omega)/P_{in,max}(\omega)$, integrated over the whole spectrum, G-BW = $\int |T| d\omega$. The G-BW that a passive matching network (PMN) can achieve is limited by the Bode-Fano bound [10], which scales with the antenna size consistent with Chu limit. To visualize this trade-off, Fig. 1a shows Q for a loop antenna with radius a and different ka (red dots). As predicted, when the loop antenna size decreases, its Q increases, lower bounded by Q_{Chu} (blue line), resulting in a smaller fractional BW. In Fig. 1b, we plot $|T|$ for the loop antenna ℵ excited with a 50Ω source through a PMN to be resonant at $f_0=kc/(2\pi)$, with c is the speed of light, and we compare it with an ideal antenna 𝔤 with $Q=Q_{Chu}$. Indeed, the G-BW of the ideal antenna is larger than the realistic loop, and its value represents the Bode-Fano bound given it is a high Q antenna [11],[12].

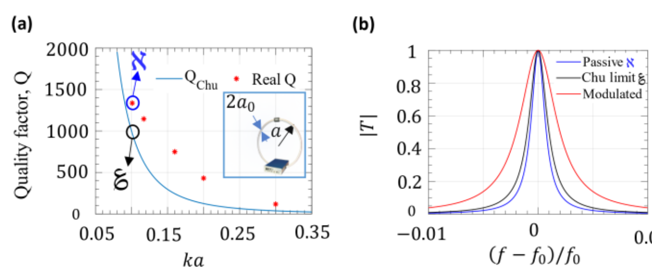

FIG. 1. (a) Small loop antenna (inset) and its quality factor, Real Q compared to Q_{Chu}. (b) $|T|$ of the loop antenna [point ℵ in (a)] matched with a PMN (blue), compared to the use of a parametric matching network modulated at $2\omega_0$ (red), and to Chu limit [point 𝔤 in (a)] (black).

Over the last decades several methods have been explored to achieve G-BW beyond the Chu limit. The most established approach is to employ active matching networks that violate Foster's reactance theorem, offering a viable path to overcome Chu limit for ESAs [13]-[16]. These solutions are also applicable to extend the BW of small resonators forming metamaterials [17],[18], leading to practical designs of wideband cloaks beyond their fundamental limitations [19]-[20]. However, this method is known to suffer from instabilities, parasitics, large noise figures, and it typically requires complex circuitry dedicated to either transmit or receive operation [15]-[21]. Alternative ways to enhance the bandwidth of ESAs are based on considering nonlinearities, e.g., using magnetized nonlinear inductors for wideband radiation and harvesting for microwaves [22]-[24] and millimeter waves [25], or wideband optical switching based on Kerr nonlinearities [26]. However, the requirements of special materials and high-power levels, in addition to inherent distortions stemming from the nonlinearity, are not compatible with most wireless applications [22]-[23]. Lastly, direct antenna modulation (DAM) techniques and antenna impedance modulation schemes have been explored to enhance the bandwidth of ESAs by breaking time-invariance [27]-[32]. In these schemes, the transient phenomena dominate the antenna performance [28], hence a direct comparison with Chu limit remains elusive, with the additional drawbacks of limited overall efficiency [30].

In this work, we explore the possibility of enabling wideband radiation enhancement beyond the Bode-Fano bound by using parametric gain enabled through periodic temporal modulations. Compared to non-Foster approaches involving amplifiers, this method is less prone to noise [33], and stability can be carefully controlled [11]. In addition, the antenna in the presented approach can operate in both transmit and receive modes [33].

Parametric gain based on temporal variations has been explored in a variety of technological platforms [35]-[41], and it is widely used in quantum computing applications [42]-[43]. The gain and linewidth of this phenomenon can be carefully controlled through the modulation properties [11],[44]. In our work, we modulate the antenna load to impart gain and broaden the bandwidth of operation, e.g., for the small loop antenna ℵ, as shown by the red curve in Fig. 1b, while at the same time ensuring stability [11].

***Theoretical analysis*—**We consider a small loop antenna, modeled by an inductance L in series with a small radiation resistance R_l [45]-[46] (as shown in shadowed orange box in Fig. 2a). In order to efficiently feed the antenna with input signal $v_{in}(t) = V_{in,0} \exp j\omega t + CC$, centered around frequency f_0, from a generator with internal real impedance R_s (as shown in shadowed blue box in Fig. 2a), we impedance match the antenna with a capacitor C_0 such that $2\pi f_0 = (LC_0)^{-1/2}$. We then modulate the capacitance in time as $C(t) = C_0 + 2MC_0 \cos(\omega_m t + \phi)$, where M is the modulation index, $\omega_m = 2\omega_0$, and ϕ is an arbitrary phase (as shown in the shadowed green box in Fig. 2a). Using Floquet theorem, the current $i(t)$ and voltage $v(t)$ across the capacitor are characterized by oscillations at frequencies Ω_0 and Ω_{-1}, where $\Omega_n = \omega + n\omega_m$, written as [47]

$$\begin{aligned} i(t) &\approx I_0 \exp j\Omega_0 t + I_{-1} \exp j\Omega_{-1} t + CC \\ v(t) &\approx V_0 \exp j\Omega_0 t + V_{-1} \exp j\Omega_{-1} t + CC \end{aligned} \quad (1)$$

and CC is the complex conjugate. Using the relation $i(t) = \frac{d}{dt}\big(C(t)v(t)\big)$, along with the circuit equations

$$\begin{aligned} V_{in,0} &= j\Omega_0 L I_0 + V_0 + I_0(R_l + R_s), \\ 0 &= j\Omega_{-1} L I_{-1} + V_{-1} + I_{-1}(R_l + R_s). \end{aligned} \quad (2)$$

we can get an expression for the input impedance $Z_{in} = V_{in,0}/I_0$ seen by the source. For $M \ll 1$, Z_{in} can be approximated as

$$Z_{in}(M) \approx (R_l + R_s) - jz_{res}\left(1 - \frac{\omega^2}{\omega_{res}^2}\right) - z_{res}\frac{M^2\omega_{res}^2}{j(\omega^2 - \omega_{res}^2) + \gamma\omega} \quad (3)$$

where $\omega_{res}^{-2} = LC_{eff}, C_{eff} = C_0(1 - M^2)$, $z_{res} = \sqrt{L/C_{eff}}$ and $\gamma = \frac{R_l + R_s}{z_{res}}\omega_{res}$. Eq. (3) shows that Z_{in} has a Drude-Lorentz lineshape with resonance frequency ω_{res} and linewidth 2γ.

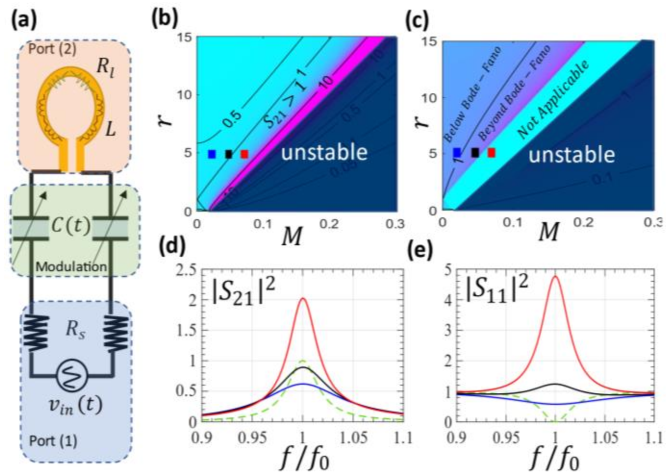

FIG. 2. (a) Circuit model for our time-modulated ESA. (b) $|S_{21}|^2$ and (c) normalized Bode-Fano integral in the parameter space $(M, R_s/R_l)$. The contour lines in correspond to constant values. (d) Squared magnitudes of scattering parameters $|S_{21}|^2$ and (e) $|S_{11}|^2$, corresponding to the three solid square symbols in (b) or (c). The dashed green line corresponds to PMN.

The effect of modulation of the input impedance is found evaluating:

$$\Delta Z_{in} = Z_{in}(M) - Z_{in}(0) = -\frac{j}{2}\sqrt{\frac{L}{C_0}}M^2\left(1 + \left(\frac{\omega}{\omega_0}\right)^2\right) - z_{res}\frac{M^2\omega_0^2}{j(\omega^2 - \omega_0^2) + \gamma\omega}$$

which has a negative real part (negative resistance) increasing with M, corresponding to the parametric gain provided by the modulation. Interestingly, for a given antenna with fixed size, i.e. fixed (L, R_l), the resonance linewidth 2γ can be independently controlled by C_0, R_s and M, which are easy to control, overcoming the strict trade-off between ESA size and bandwidth. As seen in Eq. (3), the input impedance is independent of the relative phase φ between modulation and input signal [11], other than exactly at the input frequency $\omega = \omega_0$. When $\omega = \omega_0$, the harmonics oscillating at Ω_0 and Ω_{-1} will be degenerate, i.e., oscillating at the same frequency. Therefore, in this case the relative phase between the pump and the input signal will be the prime factor in determining the gain, hence yielding a degenerate parametric amplifier, or phase sensitive parametric amplifier [48]. A small deviation for the signal frequency from ω_0, reverts the gain to be independent of the input phase, of course after averaging over a sufficiently long time that takes into account of the mismatch between modulation phase and input phase. An extended analysis of these issues is provided in Appendix A. Unlike phase-sensitive parametric amplification processes [48], where the pump energy at a single frequency relies on phase matching resulting in inherently narrowband responses, here, on the contrary, we distribute the gain over a broader frequency range, as the portion of incoming energy located exactly at $\omega = \omega_0$, and therefore sensitive to ϕ, is negligible.

Scattering matrix formalism—We model the antenna as a two-port network. At the first port we connect the excitation source, while the second port is the radiation channel (R_l), as shown in Fig. 2a. The corresponding scattering parameters for the fundamental harmonic Ω_0 are [11], [12]

$$S_{21} = \frac{2\sqrt{R_l R_s}}{Z_{in}}, S_{11} = \frac{Z_{in} - 2R_s}{Z_{in}} \qquad (4)$$

Notably, the scattering matrix is non-unitary, because of the presence of parametric gain, thus we have,

$$|S_{21}|^2 + |S_{11}|^2 = 1 - \frac{4R_s \Re\{\Delta Z_{in}\}}{|Z_{in}|^2} \geq 1, \qquad (5)$$

suggesting that the gain can be evaluated through the measurement of $|S_{11}|$. This property is useful for our experimental investigations of the antenna performance, since measuring reflections at the port is easier compared to a direct gain measurement in radiation. We stress that the spill-over of part of the incoming power into the input port is not desirable in conventional antenna operation, and it arises here because of symmetry. By including asymmetries in the modulation network, or generally choosing a more complex modulation strategy, the gain can be made directional and avoid spilling of energy into the reflection port.

We can also evaluate the Floquet scattering parameters for other harmonics, i.e., Ω_{-1} [11]. While they indicate that there is radiated power spilled into frequencies other than the signal frequency Ω_0, this undesired spill-over can be controlled with more complex modulation schemes [33]-[34].

Stability—The system becomes unstable when a complex pole, $\tilde{\omega}_p$, of the scattering parameters lies in the lower half of the complex plane under the time convention of $e^{j\omega t}$ used in this work. To determine the poles, we determine the complex zeros of the denominator in Eq. (4) corresponding to the complex zeros of Z_{in}. Using Eq. (3) and analytic continuation (as we derived the equations assuming real frequency, so to extend it to the complex plane we employ the analytic continuation to get the complex zeros of Z_{in}) we find the condition for stable operation for any input frequency to be

$$M^2 z_{res}^2 < (R_l + R_s)^2, \qquad (6)$$

which indicates that the maximum negative resistance provided by the modulation $|-M\, Z_{res}^2/(R_l+R_s)|$ needs to be smaller than the overall loss ($R_s + R_l$) in the circuit [50]. Similarly, for the degenerate case $\omega = \omega_0$ the same condition (6) should be satisfied to ensure a stable operation (see Appendix A).

The physical significance of the instability when condition (6) is not satisfied is that the harmonic amplitudes will be no more bounded, instead they grow indefinitely with time even though the values of the scattering parameters in Eq. (4) are bounded. Therefore, to analyze the circuit response beyond the stability regime, a time domain analysis should be used, highlighting the unbounded nature of the signals (see Appendix A).

Numerical results—In Fig. 2b we plot the peak of $|S_{21}|^2$ as a function of the modulation index M and the ratio $r = R_s/R_l$ where we kept constant $R_l = 4.5\Omega$ and $Q = 55$, which are close to the measured values in the parametric loop antenna experimentally studied below. In the far right of the plot, the modulation violates the inequality (6), leading to self-sustained oscillations violating stability. The contour lines correspond to different values of constant $|S_{21}|^2$, here we highlight the contour $|S_{21}|$=1 when the matching network provides parametric gain to the signal to be radiated in the region to the right. By increasing the modulation for given ratio r we increase the gain, until we hit a pole of the system and enter the unstable region.

A fundamental figure of merit to determine the performance of our modulated antenna is the Bode-Fano inequality [10]

$$\int_0^\infty - \ln\sqrt{1 - |S_{21}(\omega)|^2}\, d\omega \leq \frac{\pi R_l}{L}; |S_{21}| < 1 \qquad (7)$$

which is satisfied by any passive antenna, in compliance with Chu limit. In Fig. 2c, we show the normalized value of this integral [the ratio of the left hand side to the right hand side of (7)] for the modulated antenna. Within the stable region, small modulation amplitudes correspond to Eq. (7) being satisfied, and the antenna is narrowband. As the modulation amplitude grows, we enter the region for which the Bode-Fano limit is surpassed. As M further grows, we enter the light blue region, for which the transducer gain exceeds 1, and therefore Eq. (7) can no longer be used. This region provides even larger transducer G-BW, still ensuring stability. Our aim in this work is to explore the regime going beyond the Bode-Fano bound through parametric modulation of an electrically small loop antenna.

Fig. 2d,e show $|S_{21}|^2$ and $|S_{11}|^2$ for three representative data points in Fig. 2b or c, indicated by blue, black, and red dots. We compare these curves with the case of passive matching network (PMN) of the same antenna, i.e., for $M=0$ and $r=1$ (dashed green curve). It is shown that, as we increase M, both $|S_{11}|$ and $|S_{21}|$ increase. Later in the experimental section, we exploit this symmetry to evaluate $|S_{21}|$ by measuring the reflection $|S_{11}|$ then substituting in Eq. (5) to get $|S_{21}|$. Additionally, it is evident that the G-BW of the modulated antenna is much larger than the passive case, which we target in the experimental results.

Experimental results—To experimentally demonstrate our theoretical findings, we fabricated a small loop antenna and compared the measured $|S_{11}|$ in the passive and parametric scenarios for different modulation indexes M. We start analyzing the passive scenarios in which the antenna is matched through a PMN. Then we parametrically modulate the PMN as described above to enhance the ESA radiation. Finally, we compare the retrieved $|S_{21}|$ from both passive and modulated antennas.

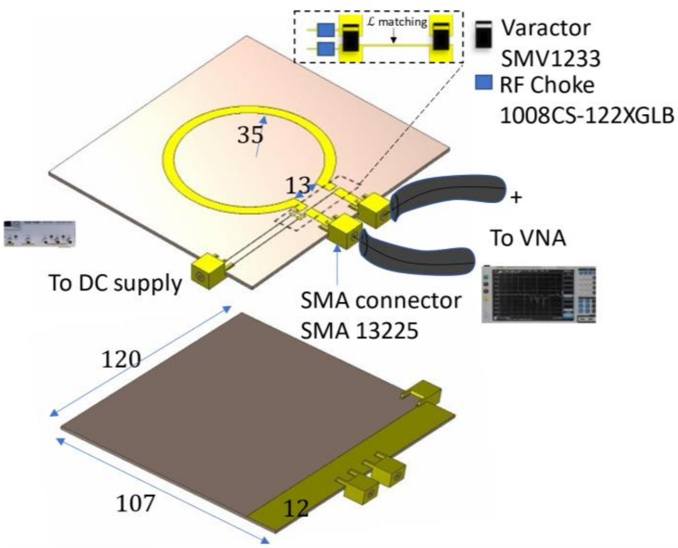

FIG. 3. 3D exploded view of the fabricated passive antenna and the experimental setup used for the passive antenna measurements with all dimensions in mm. The bottom panel shows the bottom surface of the substrate.

<u>Passive scenario</u>: We fabricated a small loop antenna on a low-loss 1.575 mm thick Rogers RT Duroid 5880 substrate of $\epsilon_r = 2.1$ and $\tan\delta$ = 0.0009. A 3D geometry of the fabricated antenna is shown in Fig. 3, where the inner radius of the loop is 35mm and the trace width is 4.5mm. To match this antenna to the generator of the vector network analyzer (VNA) with 100Ω, we employed an L matching network consisting of a shunt inductance L_m, which is realized with on-chip thin line of thickness 1 mm, as shown in the dashed box of Fig. 3, and a series capacitor formed by a varactor diode SMV1233 from Skyworks, Inc, with its capacitance tunable from 5.08pF to 1pF upon DC biasing. The varactor diode is connected to a DC feeding line through an RF choke, as shown in the dashed box, in order to prevent leakage of RF to the DC lines. In turn, the DC feeding lines are connected to a DC power supply so that we can tune the capacitance and thus the resonance frequency of the antenna as required. The two terminals of the loop antenna are connected to a vector network analyzer under excitation with power level around -40dBm to avoid triggering the varactor nonlinearity. Finally, we measure the differential S-parameters.

To illustrate the operation of the antenna in connection with an equivalent circuit model, we draw it again for consistency in the bounded box of Fig. 4 along with the half circuit model, numbering the ports. The antenna is first tuned using a PMN with equivalent circuit model ($\mathcal{L}$ matching [12] and a lumped capacitor $C(V_{DC})$), as shown in the box of Fig. 4. For this matching circuit, we use a variable capacitor $C(V_{DC})$, which will be modulated later in the parametric antenna experiment, with its static value controlled by a DC voltage source V_{DC}. In Fig. 4, we define three ports, $a, b,$ and c. Ports a and b are connected to the differential input of the VNA to excite the RF signal transmitted through the antenna, port c is instead connected to a DC supply that controls the capacitance of the varactor. In this definition, ports a and b combined define a single differential port, port 1, and the measurement results denoted as $|S_{11}|$ defines the differential-mode S-parameters, while port 2 defines the radiation channel $|S_{21}| = \sqrt{1 - |S_{11}|^2}$ when the system is lossless, which is a good assumption here because of the negligible loss introduced by the lumped elements. The differential excitation implies that ports a and b are excited by harmonics with same amplitude out of phase by π [12]. It is worth mentioning that differential-mode S-parameters are different from common-mode S-parameters. However, utilizing the circuity symmetry, we can derive differential-mode S-parameters from the common-mode S-parameters. This is done by first deriving the equivalent half circuit model, as shown in the box of Fig. 4, which has a single input port that can be used as a common-mode excitation to evaluate the S-parameters. Figure 4a,b,c plot the measured reflection coefficient for different values of V_{DC}, showing efficient tuning of the antenna resonance, with $f_0 =$ 230MHz, 290MHz, and 300MHz, as we vary $V_{DC} =$ 0, 1.5, 2.5V, respectively. In addition to the measured response, we show full-wave electromagnetic co-simulations [51]-[52] with dashed black lines, which closely agree with the measured response, with small deviations at high frequency due to parasitics and a non-accurate model of the varactor diode at high frequencies. In general, the maximum error at the resonance frequency between the measurement and the simulation results does not exceed 5%, which justifies the use of the same varactor model in all the following studies.

We performed the passive antenna measurement not only to facilitate a comparison with the parametric modulated antenna in the next section, but also to have a good estimation of the radiation resistance of the antenna, which is crucial for the Bode-Fano calculations [12]. Through the simulation model and measurement results, we can estimate the antenna radiation resistance to be R_l=0.72Ω at 230MHz and 1.2Ω at 330MHz, while the inductance of the loop L varies from 83nH at 230MHz to 120nH at 330MHz. These estimated values are based on characterizing our antenna via full-wave simulations in Fig. 3 and comparing it to the measured results. Additionally, through this comparison we can get a good estimate for the losses in the antenna that arise from lumped components and other parasitics, so we can efficiently separate the radiation resistance from the resistive loss.

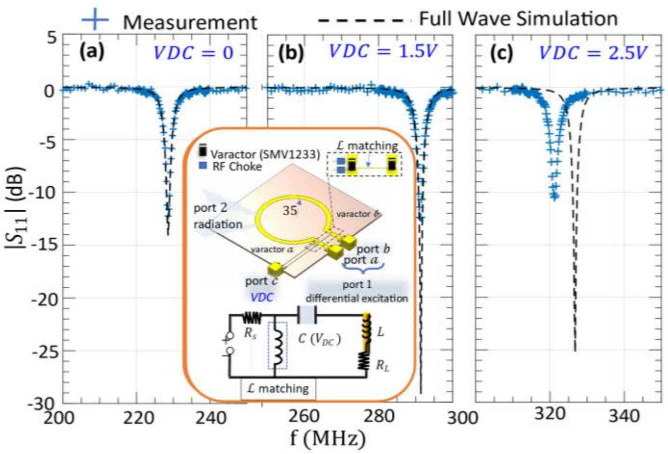

FIG. 4. (Inset) Geometry of the small loop antenna and its equivalent circuit model with dimensions in mm. The upper plane shows the top surface of the antenna with the component names and the lower plane (not shown here) has a partial ground. (a), (b), (c) Measurement and simulation results of $|S_{11}|$ for different values of $V_{DC} = (0, 1.5, 2.5)V$, respectively.

To retrieve the input impedance of the loop antenna through full-wave simulations, we calculated $Z_{loop}(circuit)$ as

$$Z_{loop}(Simulation) = Z_0 \frac{1 + S_{11}(Simulation)}{1 - S_{11}(Simulation)} = \Re Z_{loop} + j\Im Z_{loop} \quad (8)$$

where Z_0 is the internal impedance of the Vector Network Analyzer (VNA), which is 100Ω for differential measurements. The real ($\Re Z_{loop}$) and imaginary ($\Im Z_{loop}$) parts of the input impedance of the antenna are shown in Fig. 5a. We can model the input impedance in the frequency range of interest, shown by the shadowed blue region in Fig. 5a far below the first resonance of the loop at 600 MHz, as a large inductor in series with a resistance. The values of the inductor and resistor are shown in the right panel of Fig. 5a, with the caveat that for the half-circuit model, as in Fig. 4, we should use half of the values of the inductor L_{half} and radiation resistance $R_{l_{half}}$, so they are $L \approx$ (83.3,96.5,120) nH and R_l = (0.39,0.63,0.864) Ω for frequencies (240,290,330)MHz respectively, as indicated in the inset table in the right panel. Estimating the radiation resistance for the passive scenario is an important step to make a fair comparison with the modulated antenna. Therefore, to confirm the retrieved values of the antenna impedance, radiation resistance and inductance, we set up the equivalent circuit model in Fig. 4 and compare the quantity 1-$|S_{11}|^2$ from circuit simulations and from measurements. In the circuit model, we used L_m=4.92 nH and (L, R_l), with C varying based on the applied DC voltage. We compare the results for V_{DC}=0,1.5V,2.5V in Fig. 5b,c,d, respectively. Indeed, the quantity $1 - |S_{11}|^2$ from the measurement matches very well with the one obtained from the circuit model. In each case we added to the antenna radiation resistance in the table in Fig. 5a right panel, the value 0.336 Ω to provide best match between the circuit model and the measured result. This addition models the losses in the antenna that come from metal absorption and lumped component losses. When we estimate the loss for the modulated antenna (presented in the next section), we found that these parasitic losses are increased to around 3.3 Ω, due to the presence of 8 additional lumped components.

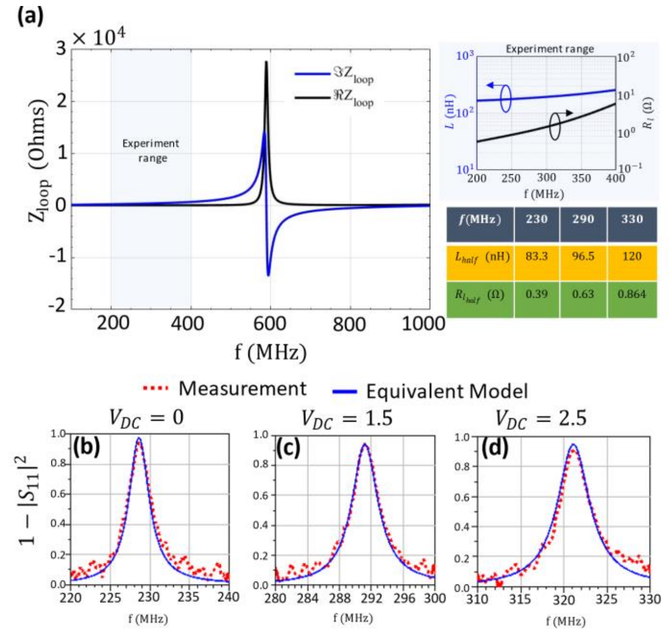

FIG. 5. Estimation of the radiation resistance and inductance. (a) Full wave simulation of the antenna impedance. The shadowed region and the inset in the right panel show the equivalent inductance and resistance value of the loop antenna at the frequency range of the experiment. (b) Measured (dashed red line) transducer gain calculated using 1-$|S_{11}|^2$, and simulated (solid blue line) gain calculated using the equivalent circuit model in Fig. 4, where the antenna parameters (L, R_l) are used from (a) and an amount of 0.336 Ω is added to the R_l to account for the losses in the antenna structure.

<u>*Modulated scenario*</u>: We fabricated the time-modulated antenna, with 3D view shown in Fig. 6. In the new setup, the small loop antenna is the same as the one in Fig. 3. However, different from the passive scenario, we have removed the thin strip that forms the matching inductor ($\mathcal{L}$ matching in the dashed box in Fig. 3). Additionally, we added a modulation network for the varactor diodes to modulate its capacitance, keeping the DC bias that provides a reverse bias V_{DC}, and hence controls the DC value of the capcitance. The modulation network consists of a filter formed by a series LC circuit at the modulation frequency ω_m [see the inset of Fig. 6], which is

connected to the two ends of the varactor diodes, and from the other two ends to the modulation feeding line. In turn, the feeding line is connected to an arbitrary waveform generator providing the sinusoidal modulation of the capacitance $V_s = V_m/2\sin\omega_m t$. Therefore, the total modulation signal is $V_s = V_{DC} + V_m/2\sin\omega_m t$, where V_{DC} and V_m control the value of C_0 and M, respectively. The AWG output is coupled to an adjustable RF amplifier (not shown) so that the amplitude of the modulation signal can be controlled. The filter at ω_m is used to prevent leakage of the RF signals provided by the VNA into the modulation network at the frequency of interest. The RF chokes for the DC bias intend to prevent leakage of both RF and modulation signals into the DC feeding lines. The top and bottom partial ground planes are connected through platted vias, as indicated by the arrows in Fig. 6, to constitute a common ground for the modulation and RF signals and to avoid grounding loops.

A real photograph of the fabricated antenna in the measurement stage is shown in the left panel of Fig. 7, and the whole structure as described can be simply modeled with an effective half circuit as seen by the VNA source due to the differential excitations, as shown in the bottom panel of Fig. 7. Notice that this simplified circuit model does not include any lumped element parasitics or SMA connector effects.

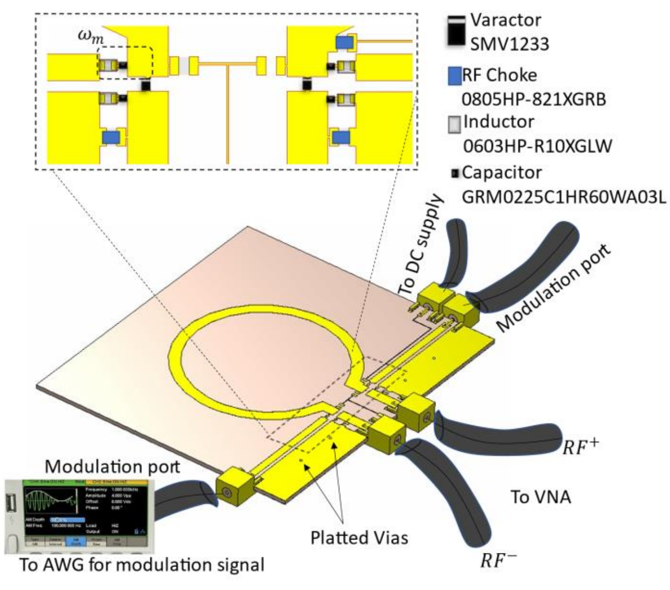

FIG. 6. 3D view of the fabricated modulated antenna and the experimental setup used for the modulated antenna. The dimensions of the antenna are the same in Fig. 3. The bottom panel of the antenna (not shown here) is similar to the botton panel of the antenna in Fig. 3.

We describe the operation of the modulated antenna In Fig. 7 as follows. We define five ports labeled a, b, c, d and e. The ports a, b, and c are similar to the three ports a, b and c in Fig. 4, with same functionalities. The additional ports d and e are added to drive the modulation signal of the capacitors on the different arms of the loop antenna. The equivalent circuit model is similar to the one in Fig. 2. Interestingly, here we completely removed the need for $\mathcal{L}$ in the PMN (see dashed box of Fig. 3), and the antenna is directly connected to the generator through the modulated varactor. In fact, we leverage the mismatch between source and load resistances to distribute the parametric effect over a broad bandwidth [11]. First, we adjust C_0 by setting the DC voltage to tune the antenna resonance to 317 MHz, yielding $ka = 0.265$ and evaluating $Q_{Chu} \approx 53$. Then, we set the modulation frequency f_m=650MHz and measured the reflection coefficient $|S_{11}|$ for $V_m = 100$mV, 750mV, corresponding to $M = 0.05, 0.17$ as shown in Fig. 7a,b, respectively. When $V_m = 100$mV, the modulation is too small to provide sufficient gain to the circuit, and we find a reflection dip at 305 MHz (consistent with the blue curve in Fig. 2c). The circuit model including parasitics and full wave simulation (red line) shows good agreement with our measurements. The retrieved circuit parameters for the antenna are $R_l = (1.2 + R_{loss})\Omega$, $L = (120 + L_1)$nH, consistent with the PMN measurements, apart from additional parasitic loss (R_{loss} =3.3Ω) and inductance ($L_1 = 5$ nH) induced by the additional lumped elements of the modulation network. By increasing the modulation amplitude to 750mV, we parametrically pump the system, and the absence of matching network controls the spreading of this gain over a broad bandwidth. This is shown as a measured reflection peak ($|S_{11}|$ >1) in Fig. 7b, again in quite good agreement with the simulation model.

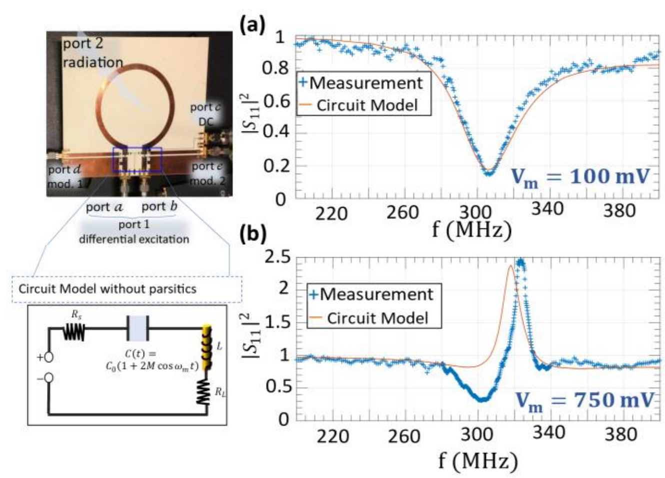

FIG. 7. (left panel) Photograph of the modulated antenna with same dimensions as in Fig. 3, the bottom box shows the effective circuit model without including any parasitics. (a), (b) Measured reflection for modulation amplitude $V_m = 100, 750$mV respectively. [$V_{DC} = 3.3$V and $\omega_m = 2\pi \times 635$MHz].

Based on the retrieved parameters from the measurement, we evaluate $|S_{21}|$ for $V_m = 750$mV, as shown in Fig. 8a (blue crosses), which surpasses the peak value in the passive case (solid red line) and provides an even broader bandwidth than what expected from an ideal antenna operating at the Bode-Fano bound with Lorentzian curve (black solid line). To evaluate this curve, we have assumed a Lorentzian line shape $\chi(f)$ such that

$$|\chi(f)|^2 = |S_{21}|^2 = \frac{1}{1+\left(\frac{f-f_0}{\sigma}\right)^2}, \quad (9)$$

where f_0 = 317MHz. We choose σ such that Eq. (7) is satisfied with the equality sign using the same values of L and R_l of the modulated antenna, and we get $\sigma \approx 5.75$MHz. The lineshape $|\chi|^2$ is the Bode-Fano transmission curve, corresponding to the best possible $|S_{21}|$ achievable with an ideal PMN.
Finally, to evaluate the actual radiated power, we performed 3D full wave multi-frequency simulations solving Maxwell's equations for the entire modulated system (see Appendix B for coupled full wave simulation details). To ease our analysis, we considered ideal parameters, i.e., neglecting parasitic and metal losses, and $V_{DC} = 0$, which results in a resonance frequency around 200MHz assuming PMN. We then excite the antenna with a peak power of 21mW, then integrate the normal component of the Poynting vector over a sphere enclosing the antenna in both the passive and modulated scenarios with increased M, as shown in Fig. 8b. As predicted, the radiated power from the modulated antenna largely exceeds the one of a passive antenna over a larger bandwidth. We further confirm this enhancement by comparing the radiation patterns in Fig. 8c, which show a conventional magnetic dipole response in all considered scenarios. In this panel, scale and color bar are the same for all antennas.

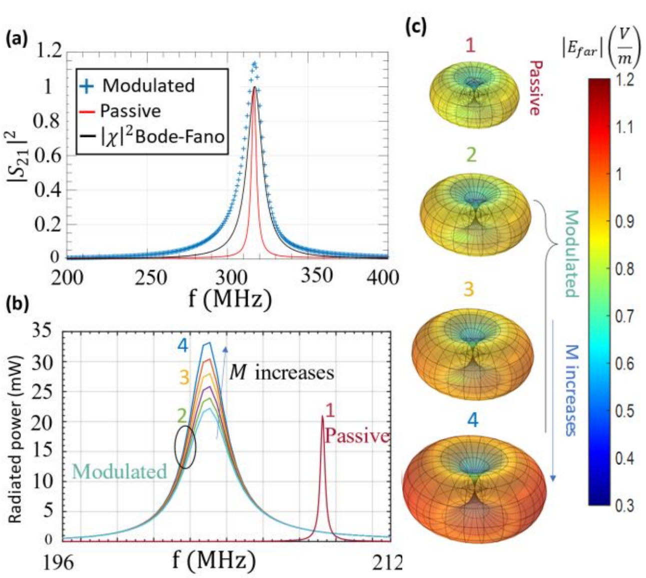

FIG. 8. (a) Comparison between $|S_{21}|^2$ for the parametric and passive antennas (retrieved from measurement), and the Bode-Fano curve $|\chi|^2$. (b) Calculated total radiated power from 3D full wave simulations for both passive and modulated antenna with 0 DC bias, an increasing modulation strength M where the maximum input power is 22mW, and (c) 3D radiation pattern of the different antennas labeled 1-4 in (b).

It is worth mentioning that there is a fundamental trade-off on the operation of the proposed parametric antenna using a single tone modulation, between the gain and 3-dB bandwidth of the system, whose product is constant [44]. This implies that a smaller fractional bandwidth is required to achieve larger gain through increasing the modulation. However, for ESA antenna applications, especially those used for medical application or in small chips, it is preferred to have higher bandwidth and no excessive gain to be within approved acceptable power ranges [53]. This is in contrast to superconducting parametric amplifiers, where both high gain and large bandwidth are desirable, since the readout signal is typically weak and requires large signal-to-noise ratios through parametric amplification [54]. These issues, together with the presence of spurious harmonics and reflected signals as already mentioned, can be addressed by considering more complex modulation schemes, for instance implementing multiple tone modulations as in superconducting quantum circuits [55].

Conclusions: In this paper, we explored and experimentally implemented parametrically enhanced radiation from ESAs, for which efficiency and bandwidth enhancements are a direct consequence of the parametric gain provided by the modulation. Compared to non-Foster circuits including amplifiers, this technique allows a better control of stability through the modulation parameters. In our experiment, we considered a planar small loop patch antenna and showed that its bandwidth can be largely increased using only a time-modulated capacitor as the matching network. We believe that this technique opens exciting opportunities for radiation enhancement through parametric phenomena for a wide range of technologies.

Acknowledgments: This work was supported by the Air Force Office of Scientific Research MURI program, the National Science Foundation EFRI program, and the Simons Foundation.

APPENDIX A: Analysis for the degenerate scenario $\omega = \omega_0$

The analysis provided in the main text assumes that the input frequency $\omega \neq \omega_0$, and it demonstrates that the response of the system is independent of the relative phase ϕ between the input and the modulation. However, for the case $\omega = \omega_0$, Eq. (2) in the main text shows that any component oscillating at $(\omega_0 - 2\omega_0)$ is not distinguishable from the component oscillating at ω_0, and thus a special treatment should be given. Since the Fourier transform $X(\omega)$ for any time domain real function $x(t)$ must satisfy the relation $X(\omega) = X^*(-\omega)$, the components I_0 oscillating at ω and the component I_{-1} oscillating at $-\omega$ must be a conjugate pair, i.e., $I_{-1} = I_0^*$. Similarly, for the voltage components, we have $V_{-1} = V_0^*$. So, one can rewrite Eq. (4) in the main text in the case of $\omega = \omega_0$ as

$$V_{in,0} = j\Omega_0 L I_0 + \frac{1}{j\Omega_0 C(1-M^2)}\left(I_0 + Me^{j\phi} I_0^*\right) + I_0(R_l + R_s). \quad \text{(A1)}$$

Assuming $I_0 = a + jb$, where $a, b \in \mathbb{R}$ and equating the real and the imaginary parts of the two sides in (A1), we can get a and b as follows,

$$a = \frac{\omega_0 C_{eff} V_{in,0}(\omega_0\tau - M\sin\phi)}{\left(\left(1-\omega_0^2 L C_{eff}\right)^2 + (\omega_0\tau)^2 - M^2\right)}$$
$$b = \frac{\omega_0 C_{eff} V_{in,0}\left(1 + M\cos\phi - \omega_0^2 L C_{eff}\right)}{\left(\left(1-\omega_0^2 L C_{eff}\right)^2 + (\omega_0\tau)^2 - M^2\right)} \quad \text{(A2)}$$

where $C_{eff} = C_0(1-M^2)$ and $\tau = C_{eff}(R_l + R_s)$. Employing $\omega_0 L C_0 = 1$, the current I_0 can be simplified as,

$$I_0 = V_{in,0}\frac{\omega C_{eff}\left((\omega\tau - M\sin\phi) + j(M^2 + M\cos\phi)\right)}{M^4 + (\omega_0\tau)^2 - M^2} \quad \text{(A3)}$$

And the degenerate input impedance $Z_{in,d} = V_{in,0}/I_{in,0}$ is given as

$$Z_{in,d} = \frac{1}{\omega C_{eff}}\frac{(\omega\tau)^2 - M^2}{(\omega_0\tau - M\sin\phi) + j(M^2 + M\cos\phi)} + \mathcal{O}(M^4). \quad \text{(A4)}$$

In fact, to evaluate the input impedance at the degenerate case, we cannot simply take the limiting case as $\omega \to \omega_0$ in Eq. (3) to get $Z_{in}(\omega \to \omega_0)$ as illustrated before, this is confirmed from Eq. (A4), it is obvious that $Z_{in}(\omega \to \omega_0) \neq Z_{in,d}$. However there is a relation between the degenerate impedance when the relative phase $\phi = 90°$, $Z_{in,d}(\phi = 90°)$ and the degenerate impedance when the relative phase $\phi = 270°$, $Z_{in,d}(\phi = 270°)$, and the impedance calculated from Eq. (3) when we take the limiting case $\omega \to \omega_0$, $Z_{in}(\omega \to \omega_0)$. First, we evaluate $Z_{in}(\omega \to \omega_0)$,

$$Z_{in}(\omega \to \omega_0) \approx R_l + R_s - \frac{z_{res}^2 M^2}{R_l + R_s},$$

then, for the degenerate case we calculate,

$$Z_{in,d}(\phi = 270°) \approx R_l + R_s - M z_{res}$$

and,

$$Z_{in,d}(\phi = 90°) \approx R_l + R_s + M z_{res}$$

So, the relation between the impedance at different phases and $Z_{in}(\omega \to \omega_0)$ is,

$$Z_{in}(\omega \to \omega_0) = \frac{z_{in,d}(\phi = 270°) z_{in,d}(\phi = 90°)}{R_l + R_s}.$$

We can calculate the scattering parameters by substituting Eq. (A3) into Eq. (4) in the main text to get,

$$|S_{21}|^2 = \frac{\left(2\omega C_0\sqrt{R_l R_s}\right)^2\left((\omega\tau)^2 + M^2 - 2\omega\tau M\sin\phi\right)}{\left((\omega_0\tau)^2 - M^2\right)^2}. \quad \text{(A5)}$$

This confirms that when $\omega = \omega_0$ the gain is phase sensitive, and it is not only a function of the modulation index M but also is a function of the relative phase between the pump and the signal, ϕ. Interestingly we see from Eq. (A5) that stability requires,

$$M < \omega_0\tau, \quad \text{(A6)}$$

which is the same condition as given in the main text knowing that $\omega_0\tau = \frac{1}{z_{res}}(R_l + R_s)$. This suggests that the circuit is always stable, given that the condition in Eq. (6) in the main text is satisfied.

To confirm the above analysis Eqn. (A1)-(A6), we perform a circuit simulation using Advanced Design System (ADS) [52]. The setup of the circuit is shown in the top panel of Fig. A1b, with the circuit parameters displayed on the circuit schematic. The setup shows a modulated capacitance with a DC capacitance C_0 and modulated with index 2M in the middle, connecting the complex load (L,R_l) on the right to the generator on the left. The DC capacitance C_0 and the load inductance L from the resonance of the circuit, $\omega_0 = 1/\sqrt{LC_0}$.

Let us assume a sinusoid input in the form of $\cos\omega t$ from the generator, where $\omega = \omega_0 = 2\pi \times 1$ GHz while the modulation frequency is set to $2\omega_0$ and has a relative phase to the input of ϕ, so the capacitance $c(t) = C_0 + 2M\cos 2\omega_0 t + \phi$. We run frequency and time domain simulations using ADS to confirm the phase dependent properties at this special degenerate case and the stability of the circuit.

In Fig. A1a, we assume a small modulation index $M = 0.02$ for which we show the frequency domain simulation results in the top and middle panels for varying phase ϕ, while the time domain results is displayed in the bottom panel at constant phase $\phi = 90°$. The scattering parameter $|S_{21}|^2$ and the input impedance $Z_{in,0}$ are shown in dashed lines in the top and middle panels, additionally, we plot the analytical results using formula (A5), (A4) respectively in the top and middle panels, in solid lines. First, we notice that the numerical and analytical results match perfectly because of the small modulation index considered. Second, it is clearly seen that the scattering parameter is a function of the phase ϕ giving the maximum gain when $\phi = 270°$, and minimum gain when $\phi = 90°$. In addition, we performed time domain simulation and record the time domain signal at the radiation resistance for $\phi = 90°, 270°$ as shown in the bottom panels of Fig. A1a, and b respectively that clearly manifests that the signal amplitude is higher when $\phi = 270°$, confirming the phase sensitive parametric amplification.

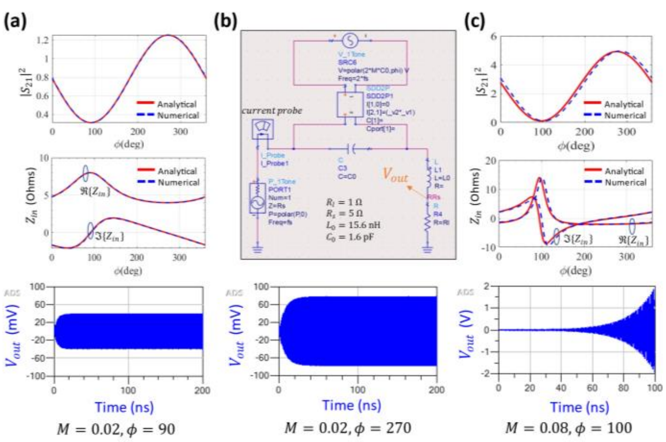

Fig. A1. (a) (top panel) Analytical and simulated results (numerical) for the scattering parameter when $M = 0.02$, (middle panel) input impedance, (bottom panel) and the time domain output signal for $\phi = 90°$. (b) The schematic of the circuit used in the simulator. (c) Similar to (a) but for M=0.08.

It is interesting to notice that the frequency domain results implied in the scattering parameters do not give information about the stability of the circuit. In fact, the scattering parameter $|S_{21}|$ can be zero from the frequency domain solver, i.e., no transmitted signal, however the circuit may be unstable. To check the stability of the circuit in Fig. A1b, we consider a higher modulation index $M = 0.08$ so it lies in the unstable region. We also plot similar results for the frequency domain solver in the top and middle panels of Fig. A1c showing good agreement with the analytical results with small shift attributed to increased modulation index. Although the scattering parameter is $|S_{21}|^2 = 0$ when $\phi \approx 90°$ as shown in Fig. A1c, the circuit is still unstable. To confirm this, we perform the time domain analysis and plot the voltage at the radiation resistance, as shown in the bottom panel of Fig. A1c which shows exponentially growing signal. Therefore, we stress that the stability of the system can be easily determined by driving it using a bounded input and observing the output. When the output is bounded, the circuit is stable, and vice versa.

APPENDIX B: COMSOL Multiphysics for time-modulated systems

We developed a full wave simulation for the modulated antenna using the finite element 3D solver, COMSOL Multiphysics [56]. This is done by first writing the current equation for the modulated capacitor, then deriving two coupled linear equations that can be solved simultaneously in COMSOL using two linear frequency domain simulations coupled through the equations derived below.

We know that the current in the capacitor oscillates with frequencies Ω_0 and Ω_{-1}. Therefore, we setup two electromagnetic wave frequency domain solvers (EMW). The first one is solved at Ω_0, and the second one is solved at Ω_{-1}. To determine the coupling between the two EMW's, we know that, $i = \frac{d}{dt}(cv)$ so we can write,

$$I_0 = j\Omega_0 C_0 V_0 + j\Omega_0 M C_0 V_{-1}$$

$$I_{-1} = j\Omega_{-1} C_0 V_{-1} + j\omega M C_0 V_0$$

where we have neglected the phase ϕ. This means that the current in the capacitor at frequency Ω_0 depends on the voltage V_0 through the conventional relation, i.e., without time modulation $I_0 = j\Omega_0 C_0 V_0$, in addition to a voltage controlled current source, i.e., the current value is controlled by the voltage V_{-1}. Similar observations can be stated for the current I_{-1}. So, the coupling is done through adding a current control voltage source to a static capacitor value of C_0. Eventually, the circuit model for the capacitance for each emw solver will be as shown in Fig. B1a. This additional voltage controlled current source can be easily implemented in COMSOL by changing the equation of the capacitance.

To evaluate the radiated power, we excite the antenna with a differential port and surround it with a perfectly matched layer to emulate the outgoing radiation boundary conditions, as shown in Fig. B1b. Then, we integrate the radiated power over the inner sphere surface of the PML, to get Fig. 8b. Notice that Fig. B1b shows the modulated antenna structure, the passive antenna is very similar except for adding an L matched network as described in Fig. 3. To get the far field radiation pattern in Fig. 8c, we used the built in Stratton-Chu formula for near field to far field transformation, where the calculated far-field electric E_{far} and magnetic H_{far} fields define the Poynting vector given by $S = Re\{E_{far} \times H_{far}^{*}\}$ where Re is the real part [56].

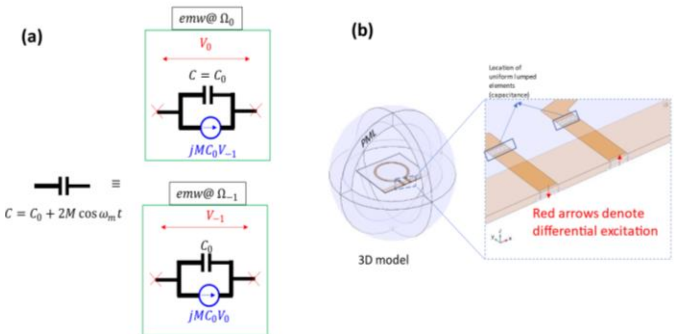

Fig. B1. (a) A periodically modulated capacitance can be solved using coupled multi-frequency simulations. In this case, we assume that only the n = 0 and n = -1 are non-negligible. Therefore, the two solvers at frequency Ω_0 and Ω_{-1} are coupled together by adding a voltage controlled current source (blue circle) (b) 3D view of the simulated antenna, and description of the placement of the lumped elements and differential port.

References

[1] V. Monebhurrun, Revision of IEEE Standard 145-2013: IEEE Standard for Definitions of Terms for Antennas [Stand on Standards], IEEE Antennas Propag. Mag. 62, 117 (2020).

[2] D. F. Sievenpiper, D. C. Dawson, M. M. Jacob, T. Kanar, S. Kim, J. Long, and R. G. Quarfoth, Experimental Validation of Performance Limits and Design Guidelines for Small Antennas, IEEE Trans. Antennas Propag. **60**, 8 (2012).

[3] A. Kiourti and K. S. Nikita, A Review of Implantable Patch Antennas for Biomedical Telemetry: Challenges and Solutions [Wireless Corner], IEEE Antennas Propag. Mag. 54, 210 (2012).

[4] H. T. Chattha, Q. H. Abbasi, M. Ur-Rehman, A. Alomainy, and F. A. Tahir, Antenna Systems for Internet of Things, Wirel. Commun. Mob. Comput. 2018, 1 (2018).

[5] Y. Huang, M. Liu, and Y. Liu, Energy-Efficient SWIPT in IoT Distributed Antenna Systems, IEEE Internet Things J. 1 (2018).

[6] H. Liu, Y. Cheng, and M. Yan, Electrically Small Loop Antenna Standing on Compact Ground in Wireless Sensor Package, IEEE Antennas Wirel. Propag. Lett. 15, 76 (2016).

[7] L. Lizzi, F. Ferrero, P. Monin, C. Danchesi, and S. Boudaud, Design of Miniature Antennas for IoT Applications, in 2016 IEEE Sixth International Conference on Communications and Electronics (ICCE) (IEEE, 2016).

[8] L. J. Chu, Physical Limitations of Omni- directional Antennas, J. Appl. Phys. 19, 1163 (1948).

[9] J. S. McLean, A Re-Examination of the Fundamental Limits on the Radiation Q of Electrically Small Antennas, IEEE Trans. Antennas Propag. 44, 672 (1996).

[10] R. M. Fano, Theoretical Limitations on the Broadband Matching of Arbitrary Impedances, J. Franklin Inst. 249, 139 (1950).

[11] H. Li, A. Mekawy, and A. Alù, Beyond Chu's Limit with Floquet Impedance Matching, Phys. Rev. Lett. 123, 164102 (2019).

[12] D. M. Pozar, Microwave Engineering, 4th ed. (John Wiley & Sons, Nashville, TN, 2012).

[13] S. E. Sussman-Fort and R. M. Rudish, Non-Foster Impedance Matching of Electrically-Small Antennas, IEEE Trans. Antennas Propag. 57, 2230 (2009).

[14] R. M. Foster, A Reactance Theorem, Bell Syst. Tech. j. 3, 259 (1924).

[15] S. D. Stearns, Incorrect Stability Criteria for Non-Foster Circuits, in Proceedings of the 2012 IEEE International Symposium on Antennas and Propagation (IEEE, 2012).

[16] M. M. Jacob, J. Long, and D. F. Sievenpiper, Broadband Non-Foster Matching of an Electrically Small Loop Antenna, in Proceedings of the 2012 IEEE International Symposium on Antennas and Propagation (IEEE, 2012).

[17] S. Hrabar, I. Krois, I. Bonic, and A. Kiricenko, Ultra-Broadband Simultaneous Superluminal Phase and Group Velocities in Non-Foster Epsilon-near-Zero Metamaterial, Appl. Phys. Lett. 102, 054108 (2013).

[18] S. Hrabar, I. Krois, I. Bonic, and A. Kiricenko, Basic concepts of active dispersionless metamaterial based on non-foster elements. In 2010 Conference Proceedings ICECom, 20th International Conference on Applied Electromagnetics and Communications (pp. 1-4). IEEE.

[19] P.-Y. Chen, C. Argyropoulos, and A. Alù, Broadening the Cloaking Bandwidth with Non-Foster Metasurfaces, Phys. Rev. Lett. 111, 233001 (2013).

[20] A. Kord, D. L. Sounas, and A. Alù, Active Microwave Cloaking Using Parity-Time-Symmetric Satellites, Phys. Rev. Appl. 10, (2018).

[21] E. Ugarte-Munoz, S. Hrabar, D. Segovia-Vargas, and A. Kiricenko, Stability of Non-Foster Reactive Elements for Use in Active Metamaterials and Antennas, IEEE Trans. Antennas Propag. 60, 3490 (2012).

[22] B. P. Mann and N. D. Sims, Energy Harvesting from the Nonlinear Oscillations of Magnetic Levitation, J. Sound Vib. 319, 515 (2009).

[23] S. Y. Karelin, V. B. Krasovitsky, I. I. Magda, V. S. Mukhin, O. G. Melezhik, and V. G. Sinitsin, Wideband RF Radiation from a Nonlinear Transmission Line with a Pre-Magnetized Ferromagnetic Core, in 2016 8th International Conference on Ultrawideband and Ultrashort Impulse Signals (UWBUSIS) (IEEE, 2016).

[24] M. Salehi and M. Manteghi, Bandwidth Enhancement Using Nonlinear Inductors, in 2011 IEEE International Symposium on Antennas and Propagation (APSURSI) (IEEE, 2011).

[25] T. Nan, H. Lin, Y. Gao, A. Matyushov, G. Yu, H. Chen, N. Sun, S. Wei, Z. Wang, M. Li, X. Wang, A. Belkessam, R. Guo, B. Chen, J. Zhou, Z. Qian, Y. Hui, M. Rinaldi, M. E. McConney, B. M. Howe, Z. Hu, J. G. Jones, G. J. Brown, and N. X. Sun, Acoustically Actuated Ultra-Compact NEMS Magnetoelectric Antennas, Nat. Commun. 8, (2017).

[26] C. Argyropoulos, P.-Y. Chen, F. Monticone, G. D'Aguanno, and A. Alù, Nonlinear Plasmonic Cloaks to Realize Giant All-Optical Scattering Switching, Phys. Rev. Lett. 108, 263905 (2012).

[27] X. J. Xu and Y. E. Wang, A Direct Antenna Modulation (DAM) Transmitter with a Switched Electrically Small Antenna, in 2010 International Workshop on Antenna Technology (IWAT) (IEEE, 2010).

[28] M. Salehi. Time-varying small antennas for wideband applications (Doctoral dissertation, Virginia Tech), 2013.

[29] M. Manteghi, A Wideband Electrically Small Transient-State Antenna, IEEE Trans. Antennas Propag. 64, 1201 (2016).

[30] W. Yao and Y. Wang, Direct Antenna Modulation - a Promise for Ultra-Wideband (UWB) Transmitting, in 2004 IEEE MTT-S International Microwave Symposium Digest (IEEE Cat. No.04CH37535) (IEEE, 2004).

[31] M. Manteghi, Antenna Miniaturization beyond the Fundamental Limits Using Impedance Modulation, in 2009 IEEE Antennas and Propagation Society International Symposium (IEEE, 2009).

[32] M. Manteghi, Non-LTI Systems, a New Frontier in Electromagnetics Theory, in 2010 IEEE Antennas and Propagation Society International Symposium (IEEE, 2010).
[33] P. Loghmannia and M. Manteghi, An Active Cavity-Backed Slot Antenna Based on a Parametric Amplifier, IEEE Trans. Antennas Propag. 67, 6325 (2019).
[34] A. Kord, D. L. Sounas, and A. Alù, Pseudo-Linear Time-Invariant Magnetless Circulators Based on Differential Spatiotemporal Modulation of Resonant Junctions, http://arxiv.org/abs/1709.08133.
[35] B. Leon, A Frequency-Domain Theory for Parametric Networks, IRE Trans. Circuit Theory 7, 321 (1960).
[36] R. Yang and H. Deng, Fabrication of the Impedance-Matched Josephson Parametric Amplifier and the Study of the Gain Profile, IEEE Trans. Appl. Supercond. 30, 1 (2020).
[37] A. Smith, R. Sandell, J. Burch, and A. Silver, Low Noise Microwave Parametric Amplifier, IEEE Trans. Magn. 21, 1022 (1985).
[38] R. W. Boyd, Nonlinear Optics (Academic Press, San Diego, CA, 1991).
[39] R. Knechtli and R. Weglein, Low-Noise Parametric Amplifier, Proc. IRE 48, 1218 (1960).
[40] M. Uenohara, M. Chruney, K. M. Eisele, D. C. Hanson, and A. L. Stillwell, 4-Gc Parametric Amplifier for Satellite Communication Ground Station Receiver, Bell Syst. Tech. j. 42, 1887 (1963).
[41] E. C. Robert, "Parametric Amplifiers," in Foundations for Microwave Engineering: Wiley-IEEE Press, 2001, p. 944.
[42] A. Metelmann and A. A. Clerk, Nonreciprocal Photon Transmission and Amplification via Reservoir Engineering, Phys. Rev. X. 5, (2015).
[43] T. Roy, S. Kundu, M. Chand, A. M. Vadiraj, A. Ranadive, N. Nehra, M. P. Patankar, J. Aumentado, A. A. Clerk, and R. Vijay, Broadband Parametric Amplification with Impedance Engineering: Beyond the Gain-Bandwidth Product, Appl. Phys. Lett. 107, 262601 (2015).
[44] H. Heffner and G. Wade, Gain, Band Width, and Noise Characteristics of the Variable- parameter Amplifier, J. Appl. Phys. 29, 1321 (1958).
[45] C. A. Balanis, Antenna Theory: Analysis and Design (Wiley-Interscience, 2014).
[46] J. E. Storer, Impedance of Thin-Wire Loop Antennas, Trans. Am. Inst. Electr. Eng. 75, 606 (1956).
[47] R. E. Collin, Foundations for Microwave Engineering, 2nd ed. (Wiley-Blackwell, Chichester, England, 2005).
[48] T. Umeki, O. Tadanaga, A. Takada, and M. Asobe, Phase Sensitive Degenerate Parametric Amplification Using Directly-Bonded PPLN Ridge Waveguides, Opt. Express 19, 6326 (2011).
[49] J. D. Jackson, Classical Electrodynamics, 3rd ed. (John Wiley & Sons, Nashville, TN, 1999).
[50] B.R. Gray. Design of RF and microwave parametric amplifiers and power upconverters (Doctoral dissertation, Georgia Institute of Technology), 2012.
[51] CST Studio Suite 3D EM Simulation and Analysis Software, https://www.cst.com..
[52] Keysight, PathWave Advanced Design System (ADS), https://www.keysight.com/us/en/products/software/pathwave-design-software/pathwave-advanced-design-system.html.
[53] A. W. Damaj, H. M. El Misilmani, and S. A. Chahine, Implantable Antennas for Biomedical Applications: An Overview on Alternative Antenna Design Methods and Challenges, in 2018 International Conference on High Performance Computing & Simulation (HPCS) (IEEE, 2018).
[54] J. Aumentado, Superconducting Parametric Amplifiers: The State of the Art in Josephson Parametric Amplifiers, IEEE Microw. Mag. 21, 45 (2020).
[55] A. Metelmann and A. A. Clerk, Quantum-Limited Amplification via Reservoir Engineering, Phys. Rev. Lett. 112, 133904 (2014).
[56] COMSOL: Multiphysics Software for Optimizing Designs, https://www.comsol.com.